photonics

MDPI

Article

Multispectral Narrowband Frustrated Total Internal Reflection Filter with Inclusions of Plasmonic Nanoparticles

Nikolai I. Petrov

Scientific and Technological Centre of Unique Instrumentation, Russian Academy of Sciences, Moscow 117342, Russia; petrovni@mail.ru

Abstract: A spatial-frequency thin-film filter with inclusions of nanoparticles operating in the visible range of the spectrum is investigated. The effect of nanoparticles embedded in the central and lateral layers of the frustrated total internal reflection filter on the spectral characteristics, considering the frequency dispersion, is investigated. It is shown that plasmonic effects cause the splitting of the filter bandwidth into a set of narrow-band spectral lines and the angular splitting of the incident beam into a set of output beams. It is demonstrated that due to the difference in the resonance conditions for *s*- and *p*-polarization waves, the spectral lines of transparency do not coincide, which indicates the possibility of using the filter as a polarizer.

Keywords: frustrated total internal reflection filter; plasmonic nanoparticles; frequency dispersion; bandwidth splitting; resonant transmission; resonant diffraction

1. Introduction

Resonance effects occur when light tunnels through a barrier system due to wave interference. Tunneling effects, which are an optical analogy of quantum mechanical tunneling, have found application in various fields of applied physics, including fiber and integrated optics, as well as frustrated total internal reflection (FTIR) spectroscopy. There are various types of devices, such as beam splitters, filters and polarizers, based on the interference of light and the frustrated total internal reflection effect in thin films.

The FTIR filter is a device based on the resonant tunneling of light through a planar dielectric optical waveguide sandwiched between two thin films with a low refractive index [1]. The theoretical description of the FTIR effect was presented long ago in [2–5]. Highly efficient FTIR-based polarization beam splitters were considered in [6,7]. It is well known that FTIR structures have transmission peaks at certain wavelengths and angles, which are very sensitive to the parameters of prisms and embedded layers. It was shown in [8] that the divergence of the incident light beam when measuring the spectral characteristics of FTIR filters should not exceed a certain limit value, which does not exceed several angular minutes. FTIR-based filtering can be used to improve the image in color display devices, color visualization systems, etc. In [9], a device was proposed for the spatial separation of an incident white light beam into three color beams. The resonant optical tunneling effect based on FTIR leads to a strong enhancement of the Goos–Hanchen shift of the light beam in graphene and plasmonic metasurfaces [10–15]. In [16], the effect of frequency dispersion in the resonator layer on the FTIR process is considered. The FTIR effect of nanoparticles embedded in the resonator layer of the filter on its transmission spectrum was investigated theoretically [16]. It was shown that the incident beam of a given wavelength is split into three angularly separated beams. The splitting of the filter bandwidth into three narrowband spectral lines for the specific incidence angle was demonstrated.

In this paper, the effect of frequency dispersion caused by silver and gold nanoparticles embedded in the central and lateral layers of the FTIR filter on the resonant transmission of

Citation: Petrov, N.I. Multispectral Narrowband Frustrated Total Internal Reflection Filter with Inclusions of Plasmonic Nanoparticles. *Photonics* **2024**, *11*, 180. https://doi.org/10.3390/photonics11020180

Received: 16 January 2024
Revised: 14 February 2024
Accepted: 14 February 2024
Published: 16 February 2024

light is investigated. In contrast to the system considered in [16], here we study the effect of plasmonic nanoparticles embedded in both the central and lateral layers. This allows us to obtain five resonant bands at once for a given angle of incidence. The influence of the polarization state of the incident beam on the transmitted spectral characteristics is also analyzed.

2. FTIR Filter

A schematic model of a filter with nanoparticle inclusions in layers is shown in Figure 1. A three-layer structure is placed between two prisms with refractive indices n_p and n'_p. The central layer with a high refractive index n_2 and thickness d_2 is sandwiched between two films with the low refractive indices n_1 and n'_1, and thicknesses d_1 and d'_1, respectively. The incident light beam undergoes chromatic and angular filtration because of resonance diffraction when light propagates through a layered structure.

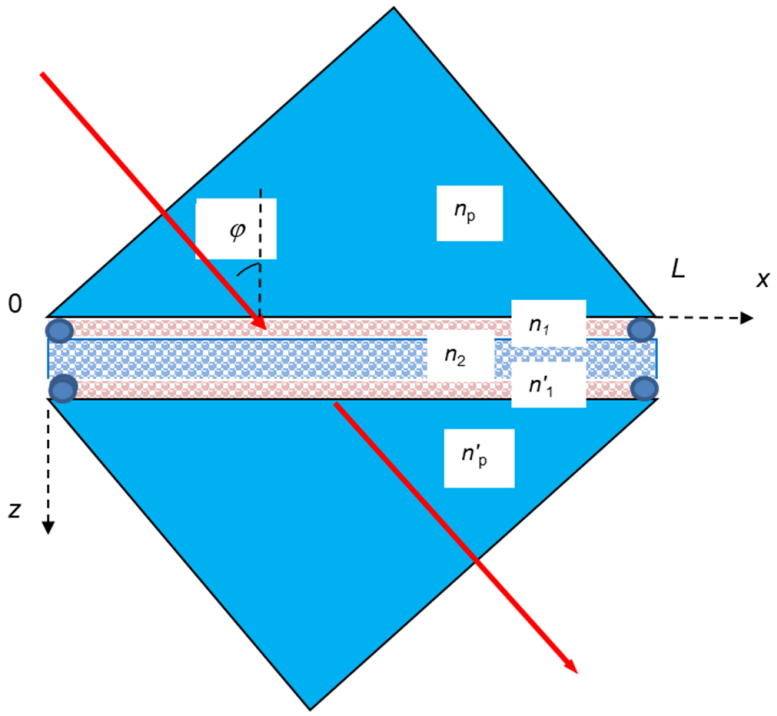

Figure 1. FTIR filter with nanoparticle inclusions in the central layer and side layers. Red arrow—incident light beam.

The differential [2] and the integral [3,4] methods can be used for the description of the frustrated total internal reflection filter. It was shown in [2] that the filter is transparent if the filter length $L > l_0 \propto tan\varphi \cdot d_2(2q_z d_1)$, where l_0 is the characteristic diffraction length, d_2 is the thickness of the central layer, d_1 is the thickness of the low-index layer, φ is the incidence angle and q_z is the imaginary part of the wave vector in a low-index layer. Using the differential method developed in [2], for the solution of the Maxwell equations, we find the local coefficient of transmittance $T(x) = |B_{out}|^2/|B_{in}|^2$, where B_{out} and B_{in} are the amplitudes of the output and incident fields, accordingly.

2.1. Resonance Condition

The resonance condition can be obtained from the solution of Maxwell's equations by taking into account the boundary conditions of continuity for the tangential components of

the field. The approximate resonance frequency in the case of the isolated central layer for the *s*-polarization is determined by the following equation [9,16]:

$$tg(k'_z d_2) = \frac{2k'_z q_z}{{k'_z}^2 - q_z^2}. \quad (1)$$

The exact resonance condition considering the influence of prisms is determined by the following equation:

$$k'_z d_2 = -arctan\left[\frac{k'_z(q_z + q'_z)}{q_z q'_z - {k'}_z^2}\right] - Q_3, \quad (2)$$

where $Q_3 = 2q_z k'_z\left(q_z^2 - k_z^2\right) exp(-2q_z d_1)/\left[\left(q_z^2 + k_z^2\right)\left(q_z^2 + {k'}_z^2\right)\right]$, $q_z = (\omega/c)\sqrt{n_p^2 \sin^2\varphi - n_1^2}$, $k_z = (\omega/c)\sqrt{n_p^2 - n_p^2 sin^2\varphi}$, $q'_z = (\omega/c)\sqrt{{n'_p}^2 \sin^2\varphi - {n'_1}^2}$, $k'_z = (\omega/c)\sqrt{n_2^2 - {n'_p}^2 sin^2\varphi}$ are the wavenumbers, ω is the frequency, c is the speed of light, and φ is the incident angle of a beam.

Thus, the exact resonance frequency will be shifted due to the influence of prisms.

The expression for the diffraction length characterizing the length of the tunnel coupling with the prism for *s*-polarization has the following form:

$$l_{0s} = \frac{1}{2}\frac{k_x}{k_z} Q_1^s Q_2^s exp(2q_z d_1) d_{2eff}, \quad (3)$$

where $d_{2eff} = d_2 + 1/q_z + 1/q'_z$, $Q_1^s = \left(q_z^2 + k_z^2\right)/(2q_z k'_z)$, $Q_2^s = \left(q_z^2 + {k'}_z^2\right)/(2q_z k'_z)$, $q'_z = \frac{\omega}{c}\sqrt{n^2 sin^2\phi - {n'_1}^2}$, $k_x = \frac{\omega}{c} n sin\phi$.

The approximate resonance condition for the *p*-polarization is expressed by the following:

$$tg(k'_z d_2) = \frac{2\left(k'_z/n_2^2\right)\left(q_z/n_1^2\right)}{{k'_z}^2/n_2^4 - q_z^2/n_1^4}. \quad (4)$$

The exact resonance condition for the *p*-polarization considering the influence of prisms is determined by the following equation:

$$k'_z d_2 = -arctan\left[\frac{k'_z\left(q_z + q'_z n_1^2/{n'_1}^2\right)}{q_z q'_z\, n_2^2/{n'_1}^2 - {k'_z}^2 n_1^2/n_2^2}\right] - \frac{2q_z k'_z\left(q_z^2 n_p^2/n_1^2 - k_z^2 n_1^2/n_p^2\right)}{\left(q_z^2 n_p^2/n_1^2 + k_z^2 n_1^2/n_p^2\right)\left(q_z^2 n_2^2/n_1^2 + {k'_z}^2 n_1^2/n_2^2\right)} exp(-2q_z d_1) \quad (5)$$

The diffraction length for the *p*-polarization has the following form:

$$l_{0p} = 0.5(k_x/k_z)\, Q_1^p Q_2^p exp(2q_z d_1)\, d_{2eff}, \quad (6)$$

where $Q_1^p = \left[q_z^2 n^2/n_1^2 + k_z^2 n_1^2/n^2\right]/(2q_z k'_z)$, $Q_2^p = \left[q_z^2 n_2^2/n_1^2 + {k'_z}^2 n_1^2/n_2^2\right]/(2q_z k'_z)$, and $d_{2eff} = d_2 + \frac{2}{q_z} \cdot \frac{\left(q_z^2 + {k'_z}^2\right)}{n_1^2 n_2^2\left(q_z^2/n_1^4 + {k'_z}^2/n_2^4\right)}$.

2.2. Transmittance

Using the differential method developed in [2], for the solution of the Maxwell equations, we find the coefficient of transmittance or transparency $T = |E_{out}|^2/|E_{in}|^2$, where E_{in} and E_{out} are the amplitudes of the incident and output fields, respectively. The transmittance bandwidth and spectral shape are determined by the deviations of the wave

vectors from their values at exact resonance (wave detuning). Provided that $\Delta\omega/\omega_0 \ll 1$ and $\Delta\varphi/\varphi_0 \ll 1$, the spectral shape of the transmitted light is defined as follows [9,16]:

$$f(\zeta) = \frac{1}{1 + l_0^2(\zeta + 1/l_r)^2}, \tag{7}$$

where l_0 is the characteristic diffraction length, $l_r = l_0 \cdot 2q_z k_z / \left(k_z^2 - q_z^2\right)$, and ζ is the integrated amount of off-resonance deviation (detuning) from the resonance frequency or resonance angle of incidence.

The wave detuning for *s*- and *p*-polarizations is defined by the following:

$$\zeta = k_z(\Delta\varphi)_\omega - k_z(\Delta\omega)_\varphi \frac{d\varphi}{d\omega}, \tag{8}$$

where $\Delta\omega = \omega - \omega_0$, $\Delta\varphi = \varphi - \varphi_0$, ω_0 and φ_0 are the resonance frequency and incident angle, accordingly.

Below, we consider a three-layer structure where $n_1' = n_1$. The angular divergence and spectral bandwidth are calculated for different refractive indices and layer thicknesses.

2.3. Dependence of Resonance Incidence Angle on Frequency

The dependence of the angle of incidence on the frequency dispersion in the case of *s*-polarization follows from the resonance condition (1):

$$\varphi(\omega) = \varphi_0(\omega) + \frac{d_2^*}{d_{2eff}} \frac{\Delta\varepsilon_2'}{n_p^2 sin2\varphi_0} + \left(1 - \frac{d_2^*}{d_{2eff}}\right) \frac{\Delta\varepsilon_1'}{n_p^2 sin2\varphi_0}, \tag{9}$$

where $\Delta\varepsilon_2'$ and $\Delta\varepsilon_1'$ are the changes in the real part of the permittivity in the central and side layers, respectively, $\varphi_0(\omega)$ is the incident angle in the absence of dispersion, $d_2^* = d_2 + 2q_z / \left(q_z^2 + k'^2_z\right)$, and $d_{2eff} = d_2 + 1/q_z + 1/q_z'$.

Note that the second term in Equation (9) relates to the dispersion in the central layer, and the third term describes the dispersion in the side layers of the filter.

A similar expression can be obtained from (4) for the *p*-polarization:

$$\varphi(\omega) = \varphi_0(\omega) + \frac{d_2^*}{d_{2eff}} \frac{\Delta\varepsilon_2'}{n_p^2 sin2\varphi_0} + \left(1 - \frac{d_2^*}{d_{2eff}}\right) \frac{\Delta\varepsilon_1'}{n_p^2 sin2\varphi_0} \frac{k_x^2 + q_z^2}{k_0^2 n_1^2}, \tag{10}$$

where $\Delta\varepsilon_2'$ and $\Delta\varepsilon_1'$ are the changes in the real part of the permittivity in the central and side layers, respectively, $\varphi_0(\omega)$ is the incident angle in the absence of dispersion, $d_2^* = d_2 + \frac{2q_z}{A}$, $A = \left[\left(\frac{q_z}{\varepsilon_1}\right)^2 + \left(\frac{k_z'}{\varepsilon_2}\right)^2\right]\varepsilon_1\varepsilon_2$, and $d_{2eff} = d_2 + \frac{2\left(q_z^2 + k_z'^2\right)}{Aq_z}$, $\varepsilon_1 = n_1^2$, $\varepsilon_2 = n_2^2$.

Here, we consider that $q_z = q_z'$, i.e., $n_1 = n_1'$.

Plasmon Resonance in Metal Nanoparticles

There are two types of plasmon modes: propagating surface plasmons and localized surface plasmons. Here we consider the localized plasmon resonances associated with metallic nanoparticles embedded into filter layers. The resonance frequency usually occurs in the visible to near-infrared spectral ranges for noble metal (Ag, Au) nanostructures [17–20]. It is assumed that the size of the nanoparticles is significantly smaller than the wavelength of light and that they are randomly distributed. In this case, the Maxwell–Garnett model can be used to describe the medium [21]. The effective dielectric constant of a medium with spherical nanoparticles satisfies the following equation [21,22]:

$$\varepsilon_{eff} = \varepsilon_m + \frac{3\eta\left(\varepsilon_p - \varepsilon_m\right)\varepsilon_m}{3\varepsilon_m + (1 - \eta)\left(\varepsilon_p - \varepsilon_m\right)}, \tag{11}$$

where ε_m is the dielectric permittivity of the central layer, ε_p is the dielectric permittivity of the nanoparticles and η is the volume fraction of nanoparticles.

In the framework of the Drude model, the optical properties of metal nanoparticles are described by the following expression:

$$\varepsilon_p(\omega) = \varepsilon_0 - \frac{\omega_p^2}{\omega^2 + i\omega\gamma}, \tag{12}$$

where ε_0 is the parameter describing the contribution of the bound electrons to the polarizability, ω_p is the plasma frequency, and γ is the damping factor of plasma oscillations. For metal nanoparticles, the damping factor γ is a size-dependent function [18,23,24]:

$$\gamma(a) = \gamma_0 + q\frac{v_F}{a}, \tag{13}$$

where v_F is the velocity of electrons at the Fermi energy, γ_0 is the damping factor for an unlimited volume of metal, and a is the radius of the nanoparticle.

3. Simulation Results

Let us now consider the effect of frequency dispersion caused by silver and gold nanoparticles embedded in the central and lateral layers of the FTIR filter on the resonant transmission of light.

3.1. s-Polarization

Figure 2 shows the dependence of the wavelength on the angle of incidence corresponding to the resonant transmission for different values of the thickness of the central layer. Only one resonant frequency corresponds to a given angle of incidence for the layers without nanoparticle inclusions. It can be seen that at a given angle of incidence, the resonant frequency increases with the increasing thickness of the central layer.

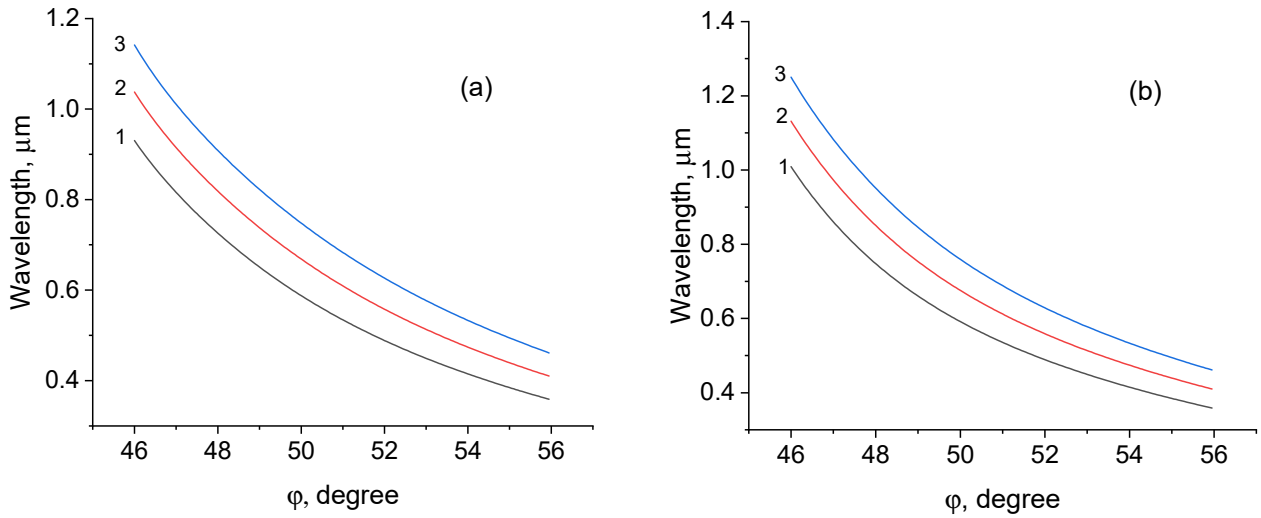

Figure 2. Resonance wavelength as a function of the incident angle for different values of central-layer thickness: 1—d_2 = 70 nm; 2—d_2 = 80 nm; 3—d_2 = 90 nm; $n_2 = 2.0$; $n_p = 2.0$; $n_1 = 1.38$; d_1 = 300 nm (**a**); d_1 = 500 nm (**b**).

When the nanoparticles are embedded into the layers, the resonance curve and transmission spectral lines are described by (9) and (7), accordingly. Figure 3 shows the dependence of the resonant angle of incidence on the wavelength of the *s*-polarized beam using the parameters for gold in the Drude model.

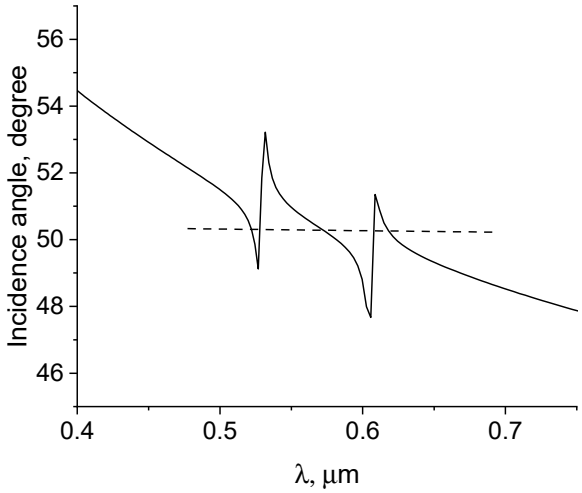

Figure 3. Dependence of the resonance incident angle of the *s*-polarized beam on the wavelength: N_p = 2.0, n_1 = 1.38, n_2 = 2.0, d_2 = 70 nm; $\eta = 10^{-3}$, d_1 = 500 nm; Au nanoparticles in the central layer and Au nanoparticles in the side layers. Dashed line corresponds to the angle of incidence of 50.26°.

It can be seen that there are two sharp changes in the behavior of the angle of incidence at wavelengths corresponding to plasmon resonances. The locations of these abrupt changes are determined by the dispersion curve of the dielectric constant in the central and lateral layers, respectively (Figure 4).

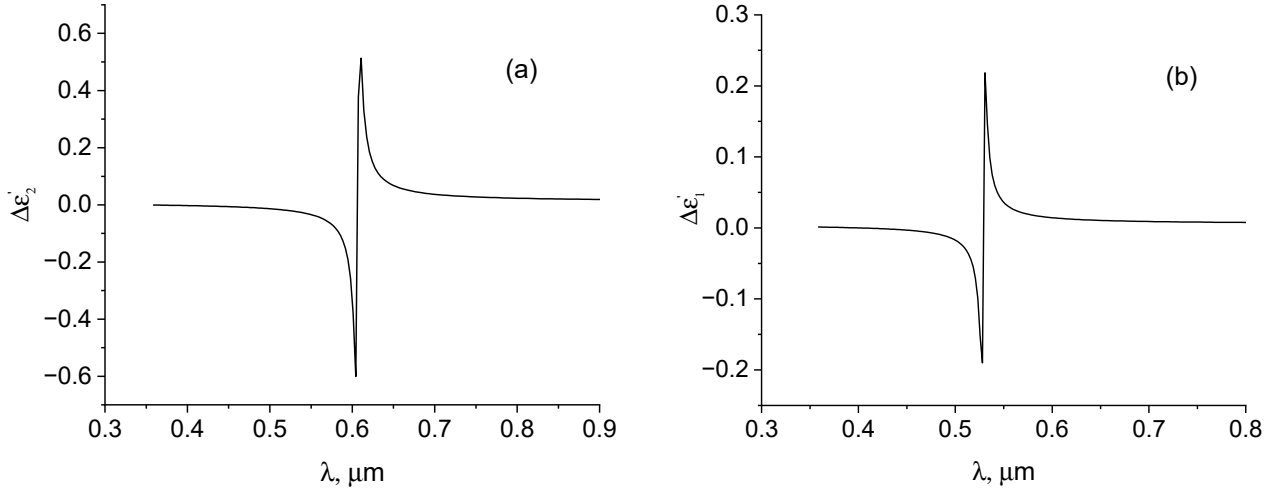

Figure 4. Dispersion curves $\Delta\varepsilon_2'$ (**a**) and $\Delta\varepsilon_1'$ (**b**) as function of wavelength.

A change in the angle of incidence leads to a change in the number of resonant wavelengths. By changing the angle of incidence, several resolved spectral lines can be obtained at the output. It follows from the simulation that the frequency dispersion of the heterogeneous layer leads to the splitting of the spectral line at a given angle of incidence in the light beam. When the angle of incidence changes, up to five resolved spectral lines can be observed at the output. As can be seen from Figure 3, at an angle of incidence in the range of 49–51°, the resonant transmission condition is satisfied simultaneously for five resonant frequencies.

In Figure 5, the spectral shapes of *s*-polarized transmitted light are shown for the central and lateral layers with gold nanoparticles. The spectral bandwidths decrease with the increase in the low-index layer thickness d_1, and the spectral line width $\Delta\lambda = 1.0$ nm was obtained at λ = 571 nm and d_1 = 500 nm (Figure 5b).

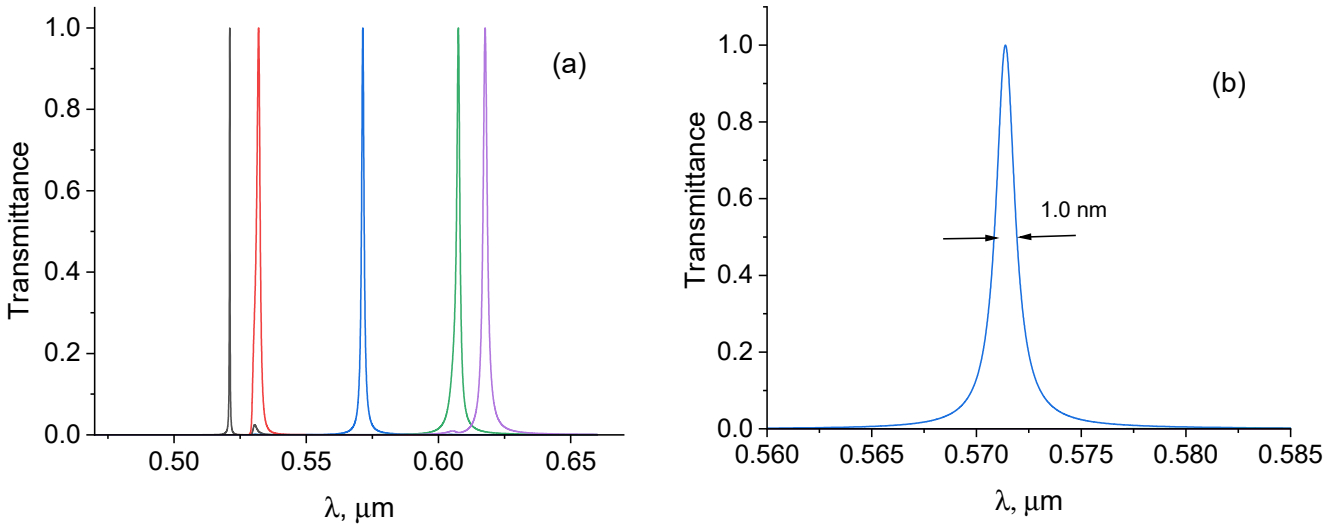

Figure 5. Spectral lines of transmitted light: $n_p = 2.0$, $n_1 = 1.38$, $n_2 = 2.0$, $d_1 = 500$ nm, $d_2 = 70$ nm, $\eta = 10^{-3}$, $\varphi = 50.26°$ (**a**), spectral line at $\lambda = 571$ nm on an enlarged scale (**b**).

Figure 6 shows the dependence of the resonant angle of incidence on the wavelength of the *s*-polarized beam for embedded *Ag* nanoparticles in the central layer and *Au* nanoparticles in the lateral layers. It is seen that five resonant wavelengths exist for a given angle of incidence (Figure 6, dashed line).

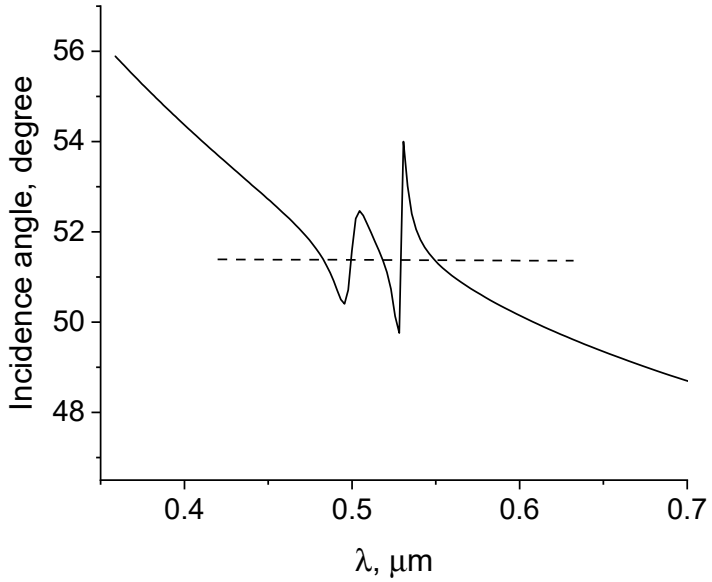

Figure 6. Dependence of the resonance incident angle of the *s*-polarized beam on the wavelength: $N_p = 2.0$, $n_1 = 1.38$, $n_2 = 2.0$, $d_2 = 70$ nm; $\eta = 10^{-3}$, $d_1 = 600$ nm; Ag nanoparticles in the central layer and Au nanoparticles in the side layers. Dashed line corresponds to the angle of incidence $\varphi = 51.49°$.

In Figure 7, the spectral lines of *s*-polarized transmitted light corresponding to the incident angle $\varphi = 51.49°$ are shown for silver nanoparticles embedded into a central layer and gold nanoparticles embedded into the lateral layers.

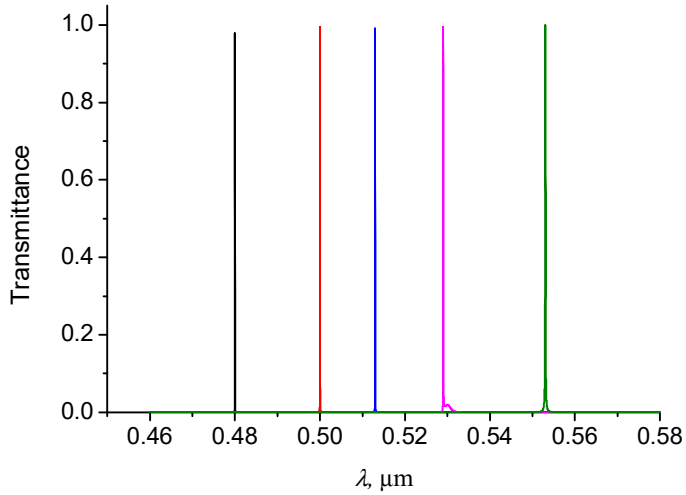

Figure 7. Spectral lines of transmitted light: $n_p = 2.0$, $n_1 = 1.38$, $n_2 = 2.0$, $d_1 = 600$ nm, $d_2 = 70$ nm, $\eta = 10^{-3}$, $\varphi = 51.49°$.

It is seen that for a given angle of incidence, there are five resonant bands at once. This indicates that the resonance condition in the resonator is satisfied for five wavelengths simultaneously. This property of the device can be applied in visualization systems. It should be noted that acousto-optic filters with inclusions of dielectric nanoparticles, considered in [22,25], also provide ultra-narrow spectral lines due to resonant Bragg diffraction on a periodic volume grating created by ultrasound in a crystal.

In Figure 8, the spectral lines corresponding to the resonant wavelengths $\lambda = 0.48$ μm (Figure 8a) and $\lambda = 0.553$ μm (Figure 8b) are presented.

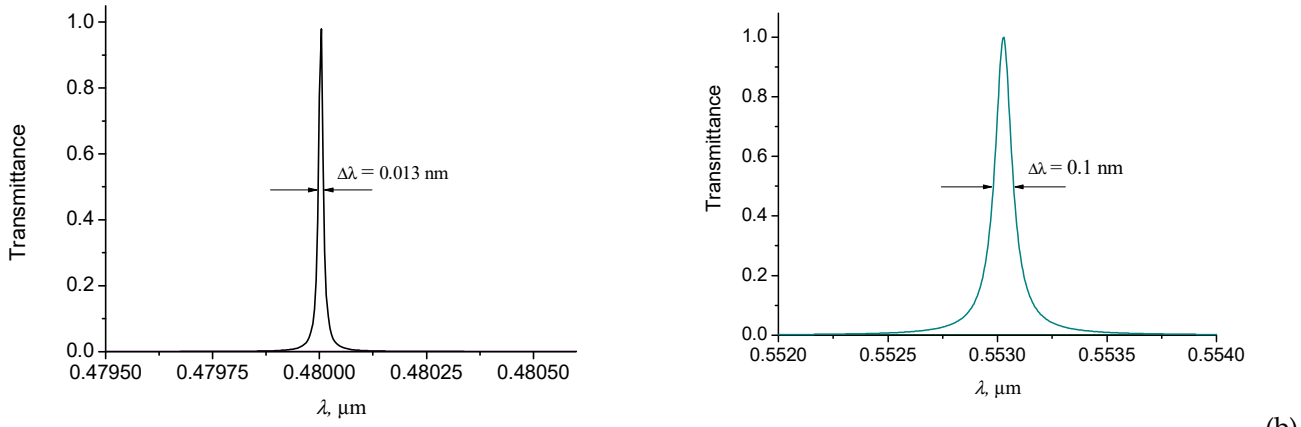

Figure 8. Spectral lines of transmitted light from Figure 6 on an enlarged scale. $\lambda = 0.48$ μm (**a**) and $\lambda = 0.553$ μm (**b**).

The width of the spectral bands decreases with decreasing wavelength, and the spectral lines with a width of $\Delta\lambda = 0.013$ nm and $\Delta\lambda = 0.1$ nm were obtained at $d_1 = 600$ nm for the central wavelengths $\lambda = 0.48$ μm and $\lambda = 0.553$ μm, respectively.

In Figure 9, the dependences of the resonant angle of incidence on the wavelength are presented for the embedded Au nanoparticles in the lateral layers. It follows that up to three resonant bands can be observed for a given angle of incidence.

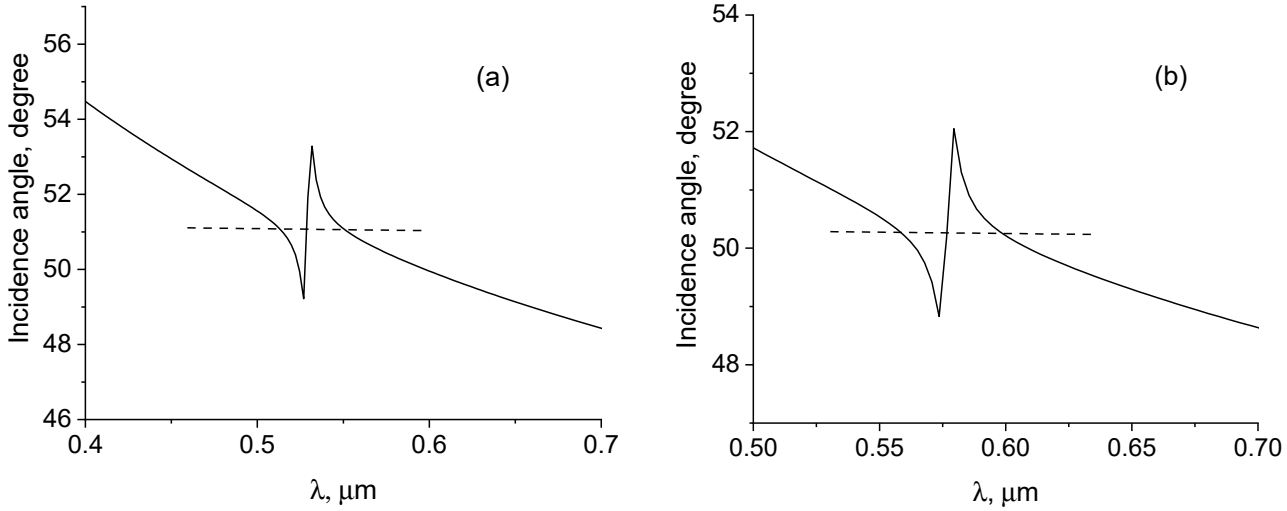

Figure 9. Resonance incident angle of *s*-polarized beam as a function of the wavelength: $n_p = 2.0$, $n_1 = 1.38$, $n_2 = 2.0$, $d_2 = 70$ nm; $\eta = 10^{-3}$, $d_1 = 300$ nm (**a**); $d_1 = 500$ nm (**b**); *Au* nanoparticles in the side layers. Dashed line corresponds to the angle of incidence $\varphi = 51.15°$ (**a**) and $\varphi = 50.27°$ (**b**).

In Figure 10, the spectral lines corresponding to the resonant incidence angles are shown for *Au* nanoparticles embedded into the lateral layers with thicknesses of 300 nm and 500 nm.

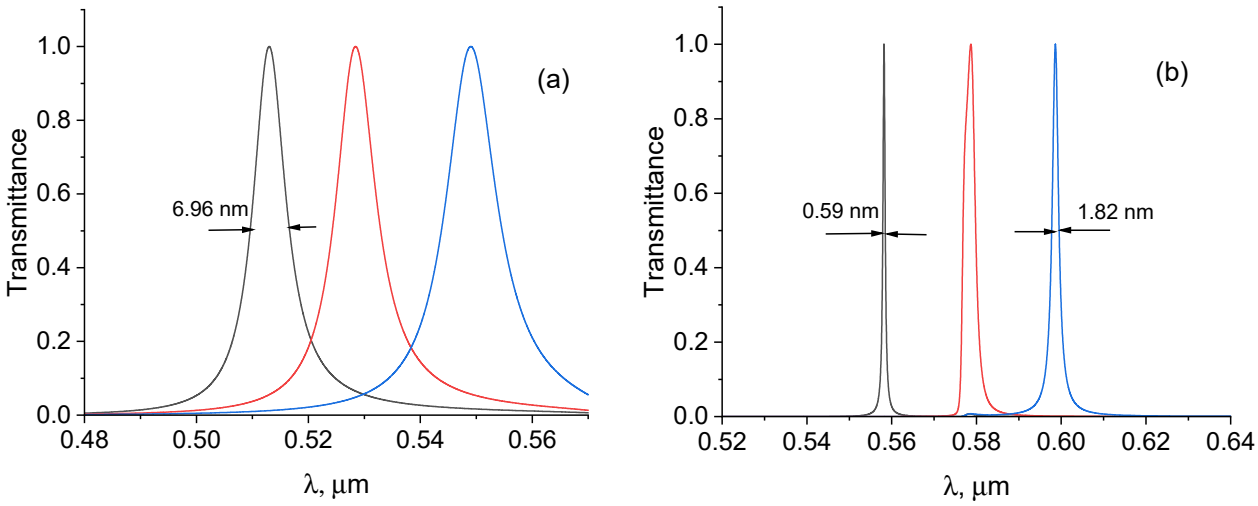

Figure 10. Spectral lines of transmitted light: $n_p = 2.0$, $n_1 = 1.38$, $n_2 = 2.0$, $d_1 = 300$ nm (**a**), $d_1 = 500$ nm (**b**), $d_2 = 70$ nm, $\eta = 10^{-3}$, $\varphi = 51.15°$ (**a**), $\varphi = 50.27°$ (**b**).

It is seen that the widths of the spectral lines decrease significantly when the thickness of the lateral layers increases.

Figure 11 shows the dependences of the resonant angles of incidence on the wavelength for embedded *Ag* nanoparticles in the lateral layers.

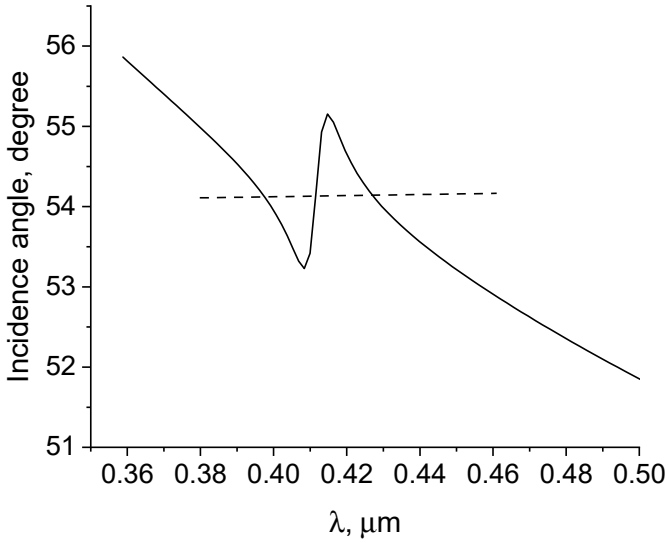

Figure 11. Dependence of the resonance incident angle of the *s*-polarized beam on the wavelength: $n_p = 2.0$, $n_1 = 1.38$, $n_2 = 2.0$, $d_2 = 70$ nm; $\eta = 10^{-3}$, $d_1 = 250$ nm; *Ag* nanoparticles in the central layer and *Au* nanoparticles in the side layers. Dashed line corresponds to the angle of incidence $\varphi = 54.11°$.

In Figure 12, the spectral lines corresponding to the resonant incidence angles are shown for *Ag* nanoparticles embedded into the lateral layers with thicknesses of 250 nm and 300 nm.

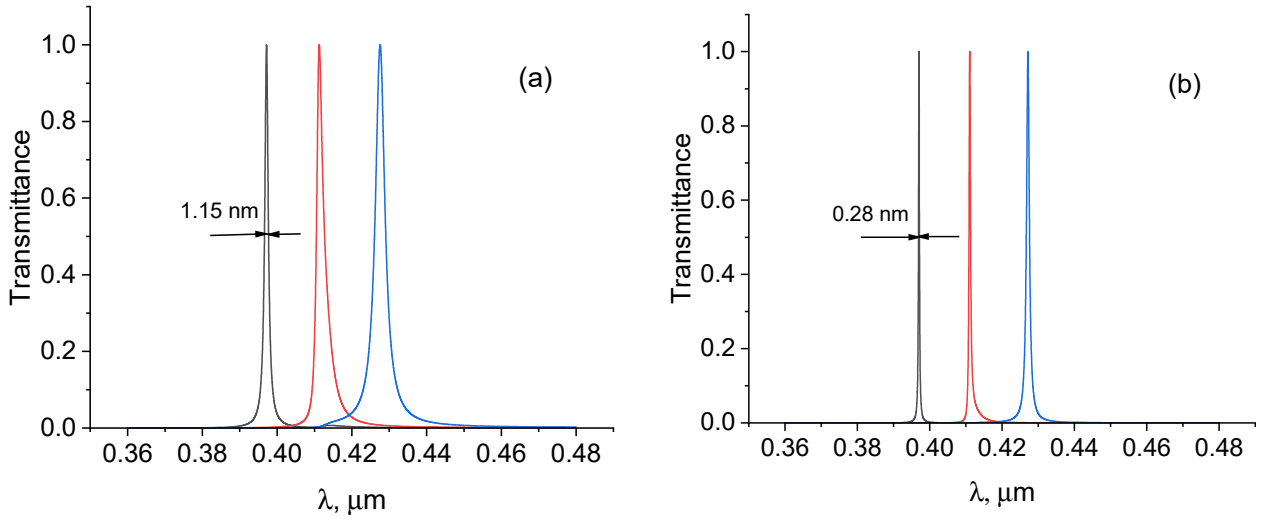

Figure 12. Spectral lines of transmitted light: $n_p = 2.0$, $n_1 = 1.38$, $n_2 = 2.0$, $d_2 = 70$ nm, $\eta = 10^{-3}$, $\varphi = 54.11°$, $d_1 = 250$ nm (**a**), $d_1 = 300$ nm (**b**).

Unlike gold nanoparticles (Figure 10), here the three resonant transmission lines are shifted to the region of short wavelengths.

3.2. p-Polarization

Figure 13 shows the dependences of the wavelength on the angle of incidence for different values of the thickness of the central layer without nanoparticle inclusions.

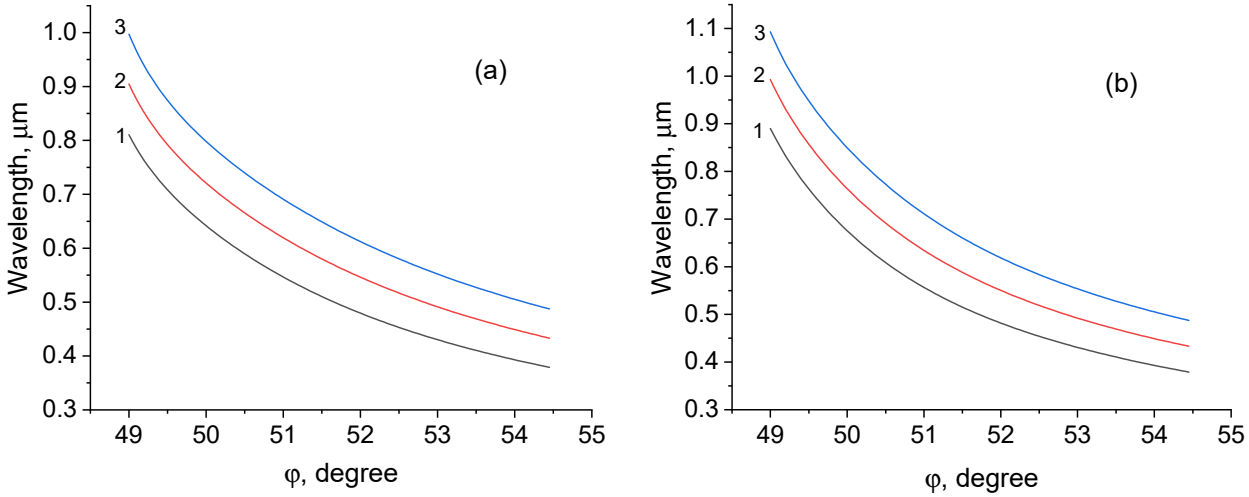

Figure 13. Dependence of resonance wavelength on incident angle of *p*-polarized beams for different values of central layer thickness: 1—d_2 = 70 nm; 2—d_2 = 80 nm; 3—d_2 = 90 nm. $n_2 = 2.0$, $n_p = 1.85$, $n_1 = 1.38$. d_1 = 300 nm (**a**), d_1 = 500 nm (**b**).

The resonance curve and transmission spectral lines in the case of the layers with embedded nanoparticles are given by (10) and (7), accordingly. Figure 14 shows the dependence of the resonant angle of incidence on the wavelength of the *p*-polarized beam for embedded *Ag* nanoparticles in the central layer and *Au* nanoparticles in the lateral layers. It is seen that five resonant wavelengths exist for a given angle of incidence (Figure 14, dashed line).

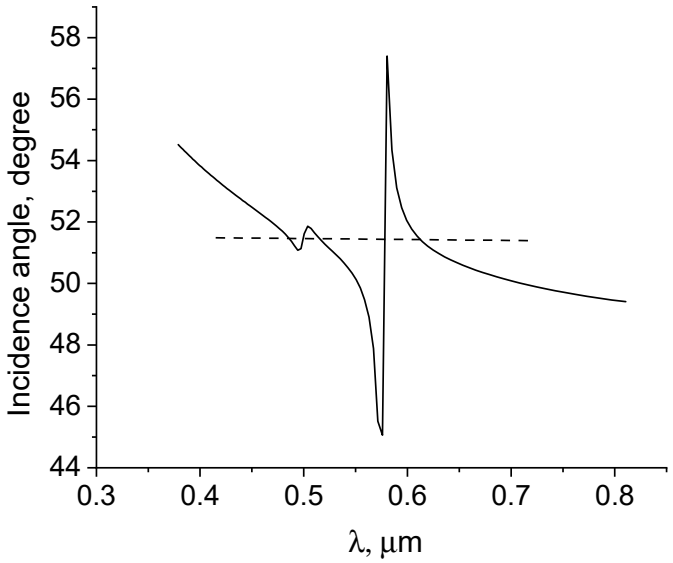

Figure 14. Dependence of the resonance incident angle of the *p*-polarized beam on the wavelength: n_p = 1.85, n_1 = 1.38, n_2 = 2.0, d_2 = 70 nm; $\eta = 10^{-3}$, d_1 = 300 nm; *Ag* nanoparticles in the central layer and *Au* nanoparticles in the side layers. Dashed line corresponds to the angle of incidence $\varphi = 51.47°$.

In Figure 15, the spectral lines of *p*-polarized transmitted light corresponding to the incident angle $\varphi = 51.47°$ are shown for silver (*Ag*) nanoparticles embedded into a central layer and gold (*Au*) nanoparticles embedded into the lateral layers.

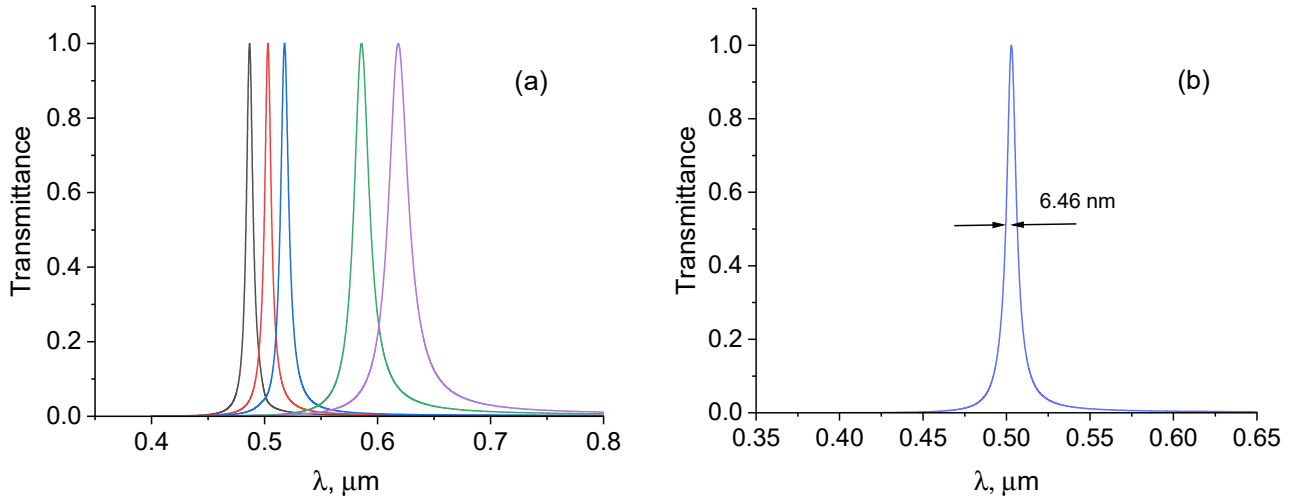

Figure 15. Spectral lines of transmitted light: n_p = 1.85, n_1 = 1.38, n_2 = 2.0, d_1 = 300 nm, d_2 = 70 nm, $\eta = 10^{-3}$, $\varphi = 51.47°$ (**a**); spectral line at λ = 518 nm on an enlarged scale (**b**).

It is seen that five resonant spectral bands exist for a given angle of incidence (Figure 14, dashed line). The spectral line width $\Delta\lambda = 6.46$ nm was obtained at λ = 518 nm and d_1 = 300 nm (Figure 15b).

In Figure 16, the spectral lines of *p*-polarized transmitted light corresponding to the incident angle $\varphi = 51.56°$ are shown for the lateral layers with a thickness of d_1= 500 nm.

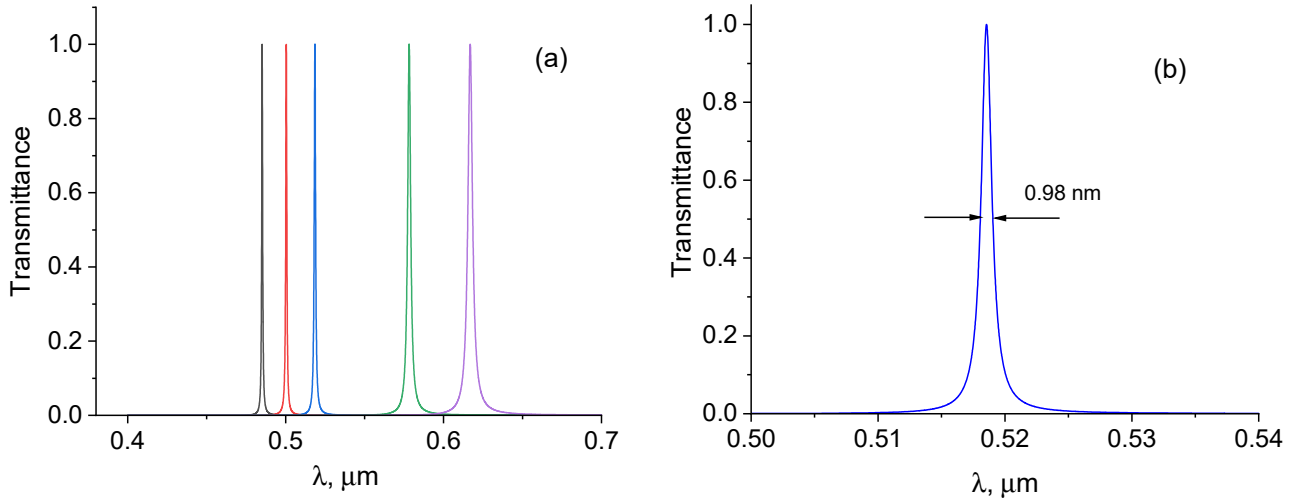

Figure 16. Dependence of the resonance incident angle of the *p*-polarized beam on the wavelength: N_p = 1.85, n_1 = 1.38, n_2 = 2.0, d_2 = 70 nm; $\eta = 10^{-3}$, d_1 = 500 nm; *Ag* nanoparticles in the central layer and *Au* nanoparticles in the side layers (**a**); spectral line at λ = 518 nm on an enlarged scale (**b**).

As can be seen, five resonant spectral bands exist for a given angle of incidence (Figure 16). The spectral line with a width of $\Delta\lambda = 0.98$ nm was obtained at d_1 = 500 nm for the central wavelength $\lambda = 518$ nm.

In Figure 17, the dependence of the resonant angle of incidence on the wavelength and the spectral lines of transmitted light are presented for embedded *Au* nanoparticles in the lateral layers. It follows that up to three resonant bands can be observed for a given angle of incidence.

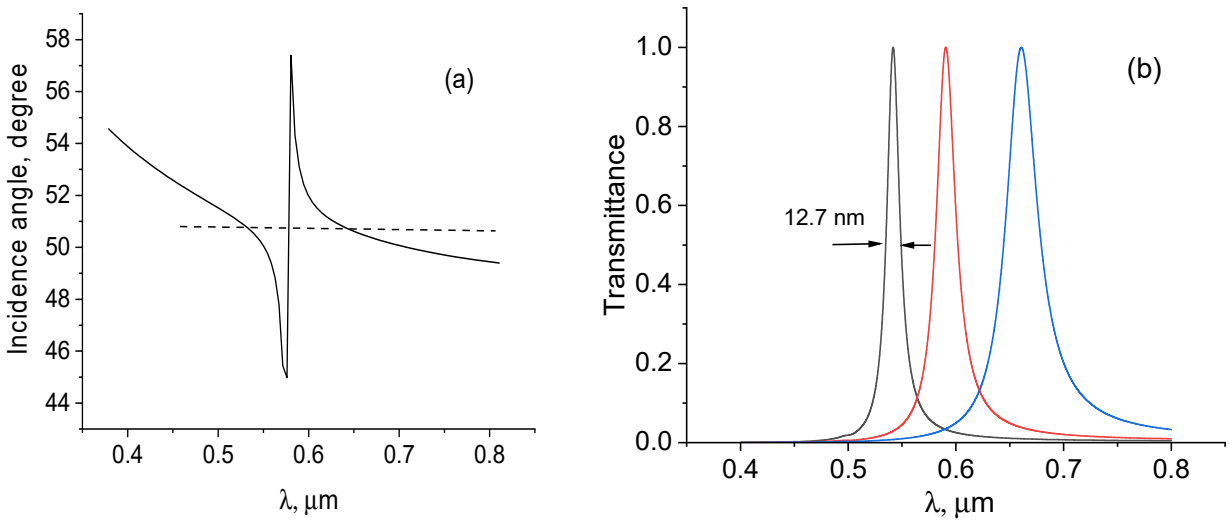

Figure 17. Dependence of the resonance incident angle of the *p*-polarized beam on the wavelength (**a**) and spectral lines (**b**): $n_p = 1.85$, $n_1 = 1.38$, $n_2 = 2.0$, $d_2 = 70$ nm; $\eta = 10^{-3}$, $d_1 = 300$ nm; *Au* nanoparticles in the side layers. Dashed line corresponds to the angle of incidence $\varphi = 50.80°$.

In Figure 18, the dependence of the resonant angle of incidence on the wavelength and the spectral lines of transmitted light are presented for embedded *Ag* nanoparticles in the lateral layers.

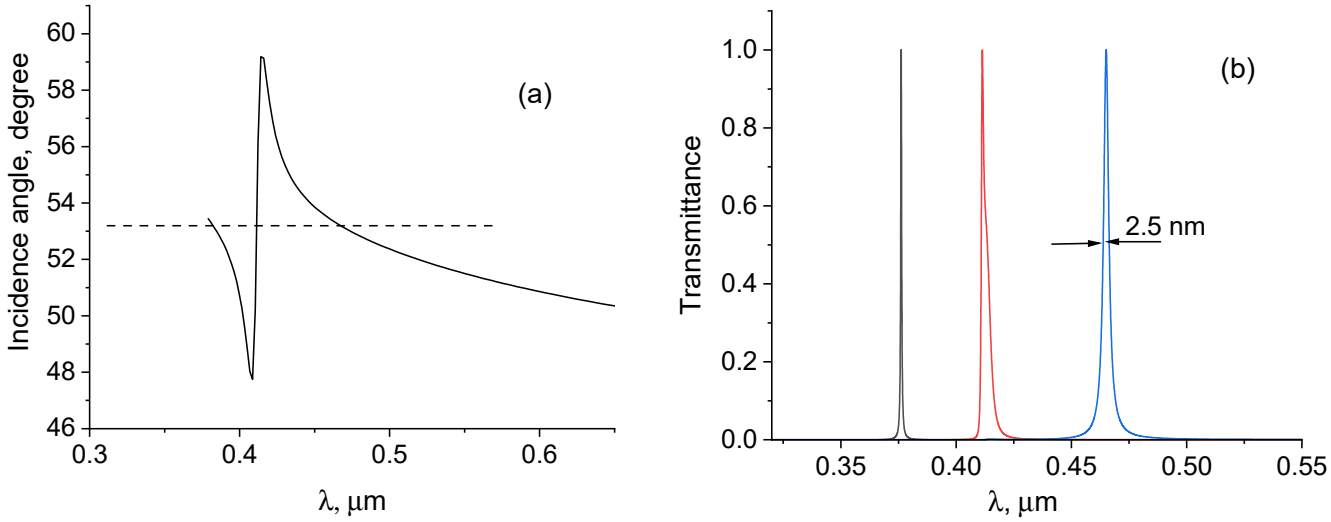

Figure 18. Dependence of the resonance incident angle of the *p*-polarized beam on the wavelength (**a**) and spectral lines (**b**): $n_p = 1.85$, $n_1 = 1.38$, $n_2 = 2.0$, $d_2 = 70$ nm; $\eta = 10^{-3}$, $d_1 = 300$ nm; *Ag* nanoparticles in the side layers. Dashed line corresponds to the angle of incidence $\varphi = 53.23°$.

It follows from the simulation that the spectral lines for layers with *Ag* nanoparticles are shifted to the region of short wavelengths compared with *Au* nanoparticles (Figure 17b). In addition, the width of the spectral lines is significantly smaller in the case of *Ag* nanoparticles. This is because plasmon resonance in *Ag* nanoparticles occurs in the short-wavelength range [16].

4. Discussion

Thus, the effect of nanoparticles embedded in the central and lateral layers of the FTIR filter on spectral characteristics, considering frequency dispersion, has been studied. The possibility of the simultaneous observation of a set of ultra-narrowband multispectral lines is demonstrated. The width of the spectral lines of such a filter decreases exponentially with

the increasing thickness of the low-index layer; therefore, ultra-narrowband transmission lines can be observed simultaneously using existing high-purity optical materials.

The combination of photonic and plasmonic resonance effects leads to spectral splitting. The key factor influencing the number and characteristics of the resulting spectral lines is the anomalous frequency dispersion caused by plasmonic nanoparticles embedded in the FTIR system. The resonant transmission of five narrow-band spectral lines near the region of anomalous dispersion at certain wavelengths has been demonstrated.

It is known that resonant diffraction phenomena can arise for wave propagation in an inhomogeneous plane-layered media, which leads to a sharp increase in the transmission of waves with a certain wavelength. In quantum mechanics, a similar effect is seen when the resonant transmission of de Broglie waves through a system of two potential barriers (the Ramsauer effect) occurs. Such phenomena take place in the propagation of waves in plasma, in the optical systems of the type of interference filters, in Fabry–Perot resonators [25,26], etc. Recently, a refractive index sensor in the terahertz domain comprising a one-dimensional photonic bandgap structure with plasmonic inclusions was proposed for opto-fluidics [27].

Recently, considerable efforts have been devoted to plasmonic and nonlinear metasurfaces [28–34]. In [28], multiple resonances of focused light beams were demonstrated experimentally in plasmonic metasurfaces supporting lattice resonances due to strong angular dispersion. In [35,36], novel physical phenomena emphasizing nanoparticle-induced non-Hermitian mode coupling and macroscopic quantum coherence in a whispering-gallery-mode optical microresonator were considered. Future research may be related to solving the problem of light diffraction in the FTIR filter, considering the spatial limitations of the incident light beam. Of particular interest is the consideration of resonant tunneling in graphene-assisted frustrated total internal reflection [37,38]. It is also of practical interest to study the effects of the spin–orbit interaction of structured light beams with orbital angular momentum and vortex partially polarized and partially coherent beams in a FTIR filter [39,40]. This will allow us to introduce an additional parameter for controlling the output data of the radiation beam, which can be used in the development of new apparatus and devices. Wide possibilities open up when using inclusions of nanoparticles with a complex shape and with special magnetic, dielectric and conductive properties.

5. Conclusions

In summary, a new FTIR filter with nanoparticles embedded in the central and lateral layers is proposed. The effect of frequency dispersion caused by silver and gold nanoparticles on the resonant transmission of the visible light of *s*- and *p*-polarizations is investigated. The resonance conditions for *s*- and *p*-polarization waves are different, so the spectral regions of transparency do not coincide. This indicates that the FTIR filter can also be used as a polarizer. The splitting of the filter bandwidth into several narrow-band spectral lines for a given angle of incidence is shown. This type of thin-film filter can be useful in many applications, including spectroscopy, sensors, in spectral regions ranging from ultraviolet to far infrared, as well as in color imaging systems.

Funding: This research was funded by the Ministry of Science and Higher Education of the Russian Federation under the State contract FFNS-2022-0009.

Institutional Review Board Statement: Not applicable.

Informed Consent Statement: Not applicable.

Data Availability Statement: Data are contained within the article.

Conflicts of Interest: The author declares no conflicts of interest.

References

1. Leurgens, P.; Turner, A.F. Frustrated total reflection interference filters. *J. Opt. Soc. Am.* **1947**, *37*, 983.
2. Iogansen, L.V. Resonance diffraction of waves in lamellar inhomogeneous media. *Sov. Phys. JETP* **1961**, *13*, 1291–1295.
3. Bergstein, L.; Shulman, C. The Frustrated total reflection filter. I. Spectral analysis. *Appl. Opt.* **1966**, *5*, 9–21. [CrossRef] [PubMed]

4. Ulrich, R. Theory of the prism–film coupler by plane-wave analysis. *J. Opt. Soc. Am.* **1970**, *60*, 1337–1350. [CrossRef]
5. Zhu, S.; Yu, A.W.; Hawley, D.; Roy, R. Frustrated Total Internal Reflection: A Demonstration and Review. *Am. J. Phys.* **1986**, *54*, 601–607. [CrossRef]
6. Azzam, R.M.A.; De, A. Circular polarization beam splitter that uses frustrated total internal reflection by an embedded symmetric achiral multilayer coating. *Opt. Lett.* **2003**, *28*, 355–357. [CrossRef] [PubMed]
7. Li, L.; Dobrowolski, J.A. Optical coatings with an integral FTIR air layer. *Opt. Express* **2010**, *18*, 3784–3792. [CrossRef]
8. Nguen, V.B.; Gubanova, L.A.; Bui, D.B. Features of the spectral characteristics of narrow-band optical filters with oblique incidence of the radiation beam. *Tech. Phys. Lett.* **2019**, *45*, 430–432. [CrossRef]
9. Petrov, N.I. Frustrated-total-internal-reflection-based thin-film color separator. *Opt. Lett.* **2007**, *32*, 2744–2746. [CrossRef]
10. Farmani, A.; Miri, M.; Sheikhi, M.H. Tunable resonant Goos–Hänchen and Imbert–Fedorov shifts in total reflection of terahertz beams from graphene plasmonic metasurfaces. *J. Opt. Soc. Am. B* **2017**, *34*, 1097–1106. [CrossRef]
11. Bocharov, A.A. Goos-Hänchen shift of a transmitted light beam in frustrated total internal reflection for moderately large gap widths. *Opt. Commun.* **2017**, *389*, 297–302. [CrossRef]
12. Xiang, L.; Liu, W.; Wei, Z.; Meng, H.; Liu, H.; Guo, J.; Zhi, Y.; Huang, Z.; Li, H.; Wang, F. Strong enhancement of Goos–Hänchen shift through the resonant optical tunneling effect. *Opt. Express* **2022**, *30*, 47338–47349. [CrossRef] [PubMed]
13. Petrov, N.I.; Sokolov, Y.M.; Stoiakin, V.V.; Danilov, V.A.; Popov, V.V.; Usievich, B.A. Observation of Giant Angular Goos-Hanchen Shifts Enhanced by Surface Plasmon Resonance in Subwavelength Grating. *Photonics* **2023**, *10*, 180. [CrossRef]
14. Fedchenko, D.P.; Kim, P.N.; Timofeev, I.V. Photonic Topological Insulator Based on Frustrated Total Internal Reflection in Array of Coupled Prism Resonators. *Symmetry* **2022**, *14*, 2673. [CrossRef]
15. Bocharov, A.A. Goos–Hänchen shift of a light beam tunable by graphene in the resonant optical tunneling structure. *J. Opt.* **2022**, *24*, 115606. [CrossRef]
16. Petrov, N.I. Splitting the bandwidth of a frustrated total internal reflection filter with nanoparticle inclusions. *OSA Cont.* **2020**, *3*, 2591–2601. [CrossRef]
17. Kelly, K.L.; Coronado, E.; Zhao, L.L.; Schatz, G.C. The optical properties of metal nanoparticles: The influence of size, shape, and dielectric environment. *J. Phys. Chem.* **2003**, *107*, 668–677. [CrossRef]
18. Kreibig, U.; Vollmer, M. *Optical Properties of Metal Clusters*; Springer: Berlin/Heidelberg, Germany, 1995.
19. Cai, W.; Shalaev, V. *Optical Metamaterials: Fundamentals and Applications*; Springer: Berlin/Heidelberg, Germany, 2010.
20. Johnson, P.B.; Christy, R.W. Optical constants of the noble metals. *Phys. Rev. B* **1972**, *6*, 4370–4379. [CrossRef]
21. Spanier, J.E.; Herman, I.P. Use of hybrid phenomenological and statistical effective-medium theories of dielectric functions to model the infrared reflectance of porous SiC films. *Phys. Rev. B* **2000**, *61*, 10437. [CrossRef]
22. Petrov, N.I.; Pustovoit, V.I. Acousto-optical properties of heterogeneous media with a nonuniform distribution of nanoparticles. *JETP Lett.* **2019**, *109*, 18–23. [CrossRef]
23. Khlebtsov, N.G. Optics and biophotonics of nanoparticles with a plasmon resonance. *Quantum Electron.* **2008**, *38*, 504–529. [CrossRef]
24. Moiseev, S.G.; Ostatochnikov, V.A. Defect modes of one-dimensional photonic-crystal structure with a resonance nanocomposite layer. *Quantum Electron.* **2016**, *46*, 743–748. [CrossRef]
25. Petrov, N.I.; Pustovoit, V.I. Small-Sized Interferometer with Fabry-Perot Resonators for Gravitational Wave Detection. *Sensors* **2021**, *21*, 1877. [CrossRef] [PubMed]
26. Isaacs, S.; Placido, F.; Abdulhalim, I. Investigation of liquid crystal Fabry-Perot tunable filters: Design, fabrication, and polarization independence. *Appl. Opt.* **2014**, *53*, H91–H101. [CrossRef] [PubMed]
27. Jose, J. Photonic bandgap structure with plasmonic inclusions for refractive index sensing in optofluidics at terahertz frequencies. *Opt. Lett.* **2017**, *42*, 470–473. [CrossRef] [PubMed]
28. Liang, Y.; Lin, H.; Lin, S.; Wu, J.; Li, W.; Meng, F.; Yang, Y.; Huang, X.; Jia, B.; Kivshar, Y. Hybrid anisotropic plasmonic metasurfaces with multiple resonances of focused light beams. *Nano Lett.* **2021**, *21*, 8917–8923. [CrossRef] [PubMed]
29. Li, Y.; Zhou, Y.; Liu, Q.; Lu, Z.; Luo, X.-Q.; Liu, W.-M.; Wang, X.-L. Multi-Wavelength Selective and Broadband Near-Infrared Plasmonic Switches in Anisotropic Plasmonic Metasurfaces. *Nanomaterials* **2023**, *13*, 3141. [CrossRef]
30. Dorrah, A.H.; Capasso, F. Tunable structured light with flat optics. *Science* **2022**, *376*, 367. [CrossRef] [PubMed]
31. Li, G.; Zhang, S.; Zentgraf, T. Nonlinear photonic metasurfaces. *Nat. Rev. Mater.* **2017**, *2*, 17010. [CrossRef]
32. Pertsch, T.; Kivshar, Y. Nonlinear optics with resonant metasurfaces. *MRS Bull.* **2020**, *45*, 210–220. [CrossRef]
33. Krasnok, A.; Tymchenko, M.; Alu, A. Nonlinear metasurfaces: A paradigm shift in nonlinear optics. *Mater. Today* **2018**, *21*, 8–21. [CrossRef]
34. Vabishchevich, P.; Kivshar, Y. Nonlinear photonics with metasurfaces. *Phot. Res.* **2023**, *11*, 850–864. [CrossRef]
35. Liu, Z.X.; You, C.; Wang, B.; Wu, Y. Nanoparticle-mediated chiral light chaos based on non-Hermitian mode coupling. *Nanoscale* **2020**, *12*, 2118–2125. [CrossRef]
36. Peng, J.X.; Jin, C.; Jin, L.; Liu, Z.X. Quantum Coherence Regulated by Nanoparticles in a Whispering-Gallery-Mode Microresonator. *Ann. Phys.* **2021**, *533*, 2100210. [CrossRef]
37. Chen, J.; Ban, Y.; Zhu, Q.B.; Chen, X. Graphene-assisted resonant transmission and enhanced Goos–Hänchen shift in a frustrated total internal reflection configuration. *Opt. Lett.* **2016**, *41*, 4468–4471. [CrossRef]

38. Tran, T.Q.; Lee, S.; Heo, H.; Kim, S. Tunable Wide-Angle Tunneling in Graphene-Assisted Frustrated Total Internal Reflection. *Sci. Rep.* **2016**, *6*, 19975. [CrossRef]
39. Petrov, N.I. Depolarization of Light in Optical Fibers: Effects of Diffraction and Spin-Orbit Interaction. *Fibers* **2021**, *9*, 34. [CrossRef]
40. Petrov, N.I. Sharp focusing of partially coherent Bessel-correlated beams by a graded-index lens. *Opt. Lett.* **2023**, *48*, 6048–6051. [CrossRef]